PAPER

Luminescence properties and its red shift of blue-emitting phosphor Na₃YSi₃O₉:Ce³⁺ for UV LED†

Luminescence properties and its red shift of blue-emitting phosphor $Na_3YSi_3O_9:Ce^{3+}$ for UV LED†

Fei Wang,[a] Wanrong Wang,[b] Liangliang Zhang,[c] Jinju Zheng,[d] Ye Jin (ID) *[a] and Jiahua Zhang[c]

A series of $Na_3YSi_3O_9:Ce^{3+}$ phosphors have been synthesized *via* a conventional high temperature solid-state reaction. Each crystal structure was characterized by X-ray diffraction (XRD) and refined by the Rietveld method. Luminescence properties of $Na_3YSi_3O_9:Ce^{3+}$ phosphors such as emission red shifts, fluorescence decay curves, thermal stability, and CIE values were systematically investigated. Upon 300 nm excitation, the emission peaks of $Na_3YSi_3O_9:Ce^{3+}$ phosphors red shift from 385 nm to 415 nm with Ce^{3+} concentration increasing from 0.002 to 0.11. Moreover, this red-shift phenomenon also occurs with an excitation wavelength from 270 nm to 340 nm as the Ce^{3+} concentration determined, which has been explained using the centroid shift and crystal field splitting. The quenching concentration of Ce^{3+} in the host $Na_3YSi_3O_9$ is determined to be about 3 mol% and the critical distance is calculated to be about 16.623 Å. The energy dispersion mechanism between Ce^{3+} ions was verified to be a dipole–dipole interaction. Temperature-dependent luminescence of $Na_3YSi_3O_9:0.03Ce^{3+}$ from 25 °C to 250 °C was evaluated, and the corresponding activation energy ΔE is 0.277 eV. Not only crystal field splitting but also centroid shift plays an important role in the red-shift of the $Na_3YSi_3O_9:Ce^{3+}$ phosphors, which may contribute to future research in designing novel solid phosphors by modifying composition of the host lattice to affect crystal field splitting and centroid shift, and then adjusting emission wavelengths to match the purposed application.

1. Introduction

As a new generation of light sources, phosphors converting white-light-emitting diodes (WLEDs) have attracted increasing attention in academic and industrial fields due to advantages such as long lifetime, saving energy, high efficiency, and environmentally friendly character.[1,2] Commercially, the most convenient way of creating WLEDs is to combine the yellow-emitting phosphor $Y_3Al_5O_{12}:Ce^{3+}$ (YAG:Ce³⁺) with blue LED chips.[3] However, owing to the lack of a red spectral component, WLEDs often have highly correlated color temperature (CCT > 4500 K) and a low color rendering index (CRI, R_a < 75).[4–7] An alternative strategy is the combination of near-UV LED chips with red-, green-, and blue-emitting phosphors as a trichromatic approach, which will produce excellent CRI values.[8] Therefore, it is very important to develop new phosphors to realize better optical requirements.

Due to its excellent thermal and chemical stability, low cost and excellent water-resistance, silicate materials have been widely studied.[9] $Na_3YSi_3O_9$ crystallized in an orthorhombic system with space group of $P2_12_12_1(19)$. These compounds possesses a mixed octahedral–tetrahedral framework, where the YO_6 octahedrals are isolated from each other by SiO_4 tetrahedrals.[10] Several research reports on $Na_3YSi_3O_9$ phosphors have been published, such as $Na_3YSi_3O_9:Bi^{3+},Eu^{3+}$ phosphor,[11] $Na_3(Y_{1−a}Ln_a)Si_3O_9$ (Ln = Eu, Tb, Tm) phosphors,[10] and $Na_3YSi_3O_9:Tm^{3+},Dy^{3+}$ phosphors.[12] On the other hand, there is little research information on the Ce³⁺ doped $Na_3YSi_3O_9$ phosphor. A Ce³⁺-activated phosphor often shows high efficiency in many hosts because of a 4f–5d parity allowed electric dipole transition. Moreover, due to the outer shell 5d orbits of Ce³⁺ ions, the emission band peak is sensitive to the host lattice,[13,14] which can be shifted from UV to the visible range; for example, the yellow-orange-emitting $CaAlSiN_3:Ce^{3+}$,[13] blue-emitting $Ca_8La_2(PO_4)_6O_2:Ce^{3+}$,[15] green-emitting $CaY_2Si_2S_8:Ce^{3+}$,[16] and yellow-emitting $LaSr_2AlO_5:Ce^{3+}$.[17,18] Herein, a series of Ce³⁺-doped $Na_3YSi_3O_9$ phosphors were synthesized *via* a conventional high temperature solid-state reaction. Crystal structures, luminescence properties, decay curves, and thermal stability were

[a]School of Science, Chongqing University of Technology, 69 Hongguang Street, Chongqing 400054, China. E-mail: jinye@cqut.edu.cn

[b]School of Electrical and Electronic Engineering, Chongqing University of Technology, 69 Hongguang Street, Chongqing 400054, China

[c]State Key Laboratory of Luminescence and Applications, Changchun Institute of Optics, Fine Mechanics and Physics, Chinese Academy of Sciences, 3888 Eastern South Lake Road, Changchun, China

[d]Institute of Materials, Ningbo University of Technology, Ningbo 315016, People's Republic of China

† Electronic supplementary information (ESI) available. See DOI: 10.1039/c7ra03813e

systematically investigated. The $Na_3YSi_3O_9$:Ce^{3+} phosphor shows blue emission and the emission band peak shifts red with increasing excitation wavelengths and Ce^{3+} content. Because electronegative vacancies affect charge distribution around the Ce^{3+} ions, the 5d energy levels shift down; thus, spectra with determined Ce^{3+} shift red and broaden under different excitation. As Ce^{3+} concentration increases, the emission shifts red and is ascribed to enhancement of the crystal field strength surrounding Ce^{3+} ions and the centroid shift of Ce^{3+} ions. Considering these factors in emission spectra, an interesting experiment may be to design solid solution phosphors *via* controlling crystal field splitting together with a centroid shift when seeking future novel phosphors.

2. Experimental section

2.1 Materials and synthesis

The $Na_3YSi_3O_9$:Ce^{3+} phosphors were prepared *via* a conventional high temperature solid-state reaction. All starting materials, *i.e.*, Na_2CO_3 (A.R.), SiO_2 (A.R.), Y_2O_3 (A.R.) and CeO_2 (4 N), were weighed according to stoichiometric ratios (Sinopharm Chemical). All raw materials were mixed and ground thoroughly in an agate mortar for 1 h, and then the homogenous mixture was put in an aluminum crucible with a cover. Next, the crucible was put in a muffle furnace with continuous sintering at 1100 °C in a reducing atmosphere for 6 h. The product was cooled down to room temperature naturally, and subsequently pulverized for further measurements.

2.2 Measurement and characterization

The crystal structure of the as-prepared phosphor was determined by X-ray diffraction (XRD) analysis using a Bruker-D8 powder diffractometer (XRD) with Cu K_α ($\lambda = 1.54078$ Å). All data were collected over a 2θ range from 10° to 80°. Room temperature excitation and emission spectra were detected using a Hitachi F-4600 spectrophotometer with a 150 W Xe lamp. Temperature-dependent luminescence properties were measure using the same spectrophotometer with a self-made heating attachment and a computer-controlled electric furnace. Decay curves were recorded on a FLS980 fluorescence spectrophotometer with a nanosecond flash nF920 as the excitation resource.

3. Results and discussion

3.1 Phase formation and crystal structure

Fig. 1 shows the XRD pattern of the as-synthesized $Na_3YSi_3O_9$:$0.03Ce^{3+}$ phosphor and the standard pattern (ICSD #20774) of $Na_3YSi_3O_9$. By comparing the diffraction peaks of XRD patterns, the XRD pattern of $Na_3YSi_3O_9$:$0.03Ce^{3+}$ agrees well with the standard pattern and no other phase is observed, demonstrating that a single phase of $Na_3YSi_3O_9$:$0.03Ce^{3+}$ phosphor has been obtained without any notable impurities. In $Na_3YSi_3O_9$, the effective ionic radii of Na^+ (CN = 6), six-coordinated Y^{3+} and four-coordinated Si^{4+} are 1.02 Å, 0.88 Å, and 0.26 Å, while the ionic radii of Ce^{3+} is 1.01 Å. Considering

the ionic radii differences between the doped ions and cations, there may a be potential for Ce^{3+} ions to occupy both Na^+ sites and Y^{3+} sites in $Na_3YSi_3O_9$. In fact, according to Bragg's equation $2d \sin\theta = n\lambda$, the shrinkage of cell volume will lead to an increase of the 2-theta value. When a larger cation is replaced by smaller doping ions, the 2-theta value shifts right.[19] The main diffraction peaks shift to a higher angle in the enlarged view from 20° to 35° (Fig. 1), which indicates that Ce^{3+} ions substituted the position of Na^+ sites in the $Na_3YSi_3O_9$ host lattice.

To further understand phase purity and occupancy of Ce^{3+} ions, a Rietveld structure refinement of the as-prepared sample was performed using the general structure analysis system (GSAS) program as shown in Fig. 2a.[20] The standard $Na_3YSi_3O_9$ was used as an initial structure model, and the refined parameters, residual factors of un-doped $Na_3YSi_3O_9$ and $Na_3YSi_3O_9$:$0.03Ce^{3+}$ are summarized in Table 1. Results of the Rietveld refinement further demonstrate that the doping of Ce^{3+} ions did not generate any impurity in $Na_3YSi_3O_9$. Un-doped $Na_3YSi_3O_9$ and $Na_3YSi_3O_9$:$0.03Ce^{3+}$ crystallized in an orthorhombic system with a space group of $P2_12_12_1(19)$, and the lattice parameters for $Na_3YSi_3O_9$:$0.03Ce^{3+}$ were fitted to be $a = 15.0363(4)$ Å, $b = 15.1427(5)$ Å, $c = 15.2095(3)$ Å, $\alpha = \beta = \gamma = 90°$, $V = 3463.08(5)$ Å^3, and $Z = 16$, and the reliability factors are $\chi^2 = 7.048$, $R_{wp} = 17.37\%$ and $R_p = 12.81\%$, while the parameters for un-doped $Na_3YSi_3O_9$ are $a = 15.0384(1)$ Å, $b = 15.1478(0)$ Å, $c = 15.2135(9)$ Å, $\alpha = \beta = \gamma = 90°$, $V = 3465.64(0)$ Å^3, $Z = 16$, $\chi^2 = 6.560$, $R_{wp} = 17.01\%$, $R_p = 12.95\%$. Comparing the refined parameters of $Na_3YSi_3O_9$:$0.03Ce^{3+}$ with the parameters of un-doped $Na_3YSi_3O_9$, we observed that values of the refined parameters were smaller after doping Ce^{3+} ions, which is caused by the fact that the larger host cations were replaced by smaller doping ions. The atomic occupancy of Ce and Na is provided in Table S1 in the ESI† which further confirmed that Ce^{3+} ions occupied the six-coordinated Na^+ sites. Fig. 2b presents the coordination spheres of six-coordinated Na^+ ions, forming distorted octahedrons with Si^{4+} ions coordinated by four oxygen atoms in a regular tetrahedron and the Y^{3+} ions in regular $[YO_6]^{9-}$ octahedrons along the *a*-direction. The distorted $[NaO_6]^{11-}$ octahedron connected with the $[SiO_4]^{4-}$ tetrahedron and $[YO_6]^{9-}$ octahedron by sharing edges or corners to form a three-dimensional framework. Moreover, the distorted $[NaO_6]^{11-}$ octahedron connected with another six-coordinated Na^+ ion by the O^{2-} point.

3.2 Photoluminescence properties and the red-shift emissions of $Na_3YSi_3O_9$:Ce^{3+} phosphors

Photoluminescence emission (PL, $\lambda_{ex} = 300$ nm) and excitation (PLE, $\lambda_{em} = 402$ nm) spectra of $Na_3YSi_3O_9$:$0.03Ce^{3+}$ are depicted in Fig. 3a. The PLE spectrum represents a broad hump from 240 nm to 375 nm, assigned to electron transition from the 4f energy level to different 5d sub-levels of Ce^{3+} ions. Upon 300 nm excitation, the $Na_3YSi_3O_9$:$0.03Ce^{3+}$ phosphor shows a broad emission band from 340 nm to 570 nm peaking at 402 nm, which is attributed to the spin-allowed 5d–4f transitions of Ce^{3+} ions. For the sake of clarity, the PL asymmetric band de-
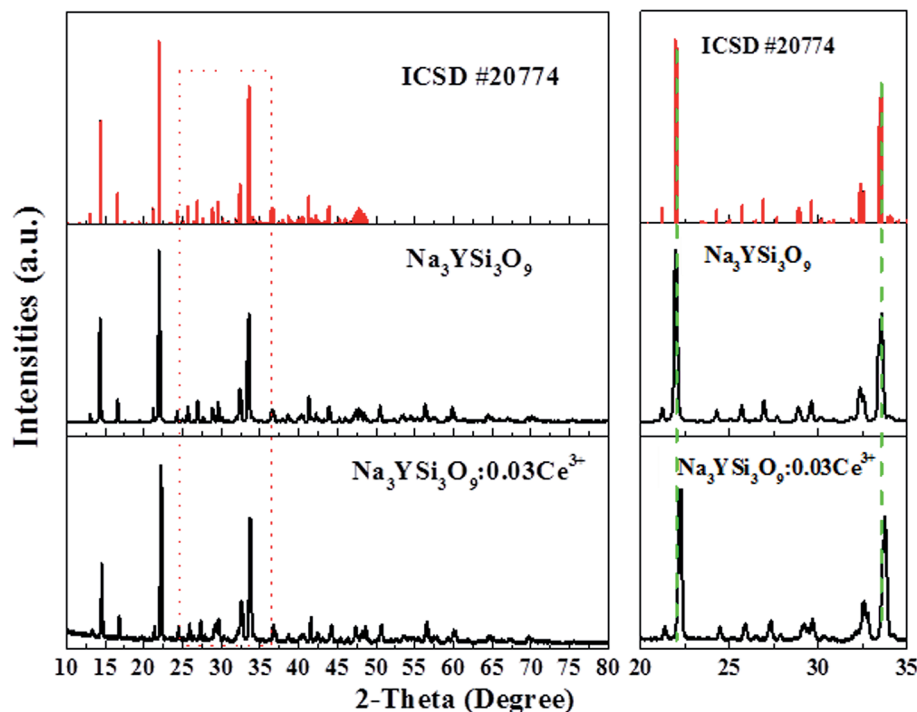
Fig. 1 Powder XRD pattern of the $Na_3YSi_3O_9$:$0.03Ce^{3+}$ phosphor with the standard pattern (ICSD #20774).

convoluted by Gaussian functions fit with good approximation with two Gaussian curves peaking at 23 490 cm^{-1} (~425 nm) and 25 544 cm^{-1} (~391 nm), as shown in Fig. 3b. The energy difference was calculated to be 2054 cm^{-1}, which is close to that between $^2F_{5/2}$ and $^2F_{7/2}$ (generally $\approx$ 2000 cm^{-1}).[21] Herein, the two Gaussian peaks are ascribed for the transitions from the lowest 5d excited state to the $^2F_{5/2}$ and $^2F_{7/2}$ ground states of Ce^{3+} ions due to spin–orbit coupling. That is to say, there exists only one type of emission center in the $Na_3YSi_3O_9$ host lattice, which is consistent with Ce^{3+} ion substituting the six-coordinated Na^+ site in $Na_3YSi_3O_9$.

Fig. 4a and b present the PL spectra of $Na_3YSi_3O_9$:$0.03Ce^{3+}$ and $Na_3YSi_3O_9$:$0.09Ce^{3+}$ excited with various excitation wavelengths, respectively. The emission of $Na_3YSi_3O_9$:xCe^{3+} samples excited under different wavelengths (270–340 nm) are shown in Fig. S1 and a summary is listed in Table S2.† When the excitation wavelength gradually increased from 270 nm to 340 nm, the emission of $Na_3YSi_3O_9$:$0.03Ce^{3+}$ shifted to longer wavelengths from 398 nm to 418 nm, and the emissions of $Na_3YSi_3O_9$:$0.09Ce^{3+}$ shifted from 411 nm to 431 nm. Here, due to the fixed Ce^{3+} concentration, the explanation of the red shift by crystal field splitting is excluded. The ~20 nm red shift is supposed to be ascribed to a 5d centroid shift of Ce^{3+}. Because of different valence states and the charge mismatch originating from doping ions Ce^{3+} on the Na^+ site in $Na_3YSi_3O_9$, two vacancies with one Ce^{3+} ion would exist according to the formal equation: $Ce^{3+} \xrightarrow{Na^+} Ce_{Na}^{\cdot\cdot} + 2V'_{Na}$.[22] Vacancies with a charge would appear because of the different valence states and the possible charge compensation behavior originating from Ce^{3+} ions substituting for the Na^+ sites. Meanwhile, the

electronegative vacancies will affect charge distribution with its chemical environment around the Ce^{3+} ion, and is reflected by the centroid shift with 5d levels of Ce^{3+}.[23] Since the bond length and bond angle of six-coordinated Na^+ are different, as shown in Fig. 2b, the effect of vacancies on Ce^{3+} could not be always identical to all doping Ce^{3+} ions in $Na_3YSi_3O_9$. Therefore, the effect of these vacancies not only shifts down the centroid of 5d levels leading to the emission red shift, but also broadens the spectra (Fig. 4).

Fig. 5 illustrates the PL spectra of $Na_3YSi_3O_9$ with different Ce^{3+} ion concentrations under 300 nm excitation. Except for intensity, the PL spectra of $Na_3YSi_3O_9$:xCe^{3+} (x = 0.002, 0.01, 0.03, 0.05, 0.07, 0.09, and 0.11) have similar spectral profiles with a continuous 30 nm red-shift of Ce^{3+} emission from 385 nm to 415 nm as the concentration of Ce^{3+} increases gradually, exhibiting a larger shift than that of Fig. 4a and b.

Comparing the 20 nm red shift of the 5d centroid shift in Fig. 4 with the 30 nm red-shift of the Ce^{3+} emission as the concentration of Ce^{3+} increased in Fig. 5, the difference of that red shift should be noted. Mostly, the emission shift phenomenon results from a crystal field splitting effect as referenced in other works.[24–26] Therefore in this paper, not only crystal field splitting should be considered, but the centroid shift should be also taken into account with the red shift.

It is established that the Dieke diagram of 4f energy levels is almost invariant while the energies of 5d states are influenced 50 times stronger by the host compound than those of 4f states.[27] When lanthanide ions are present in a compound, the lowest level of the 5d configuration would shift down as the emission shifted red. The down shift $D(3+,A)$ of the first 4f–5d
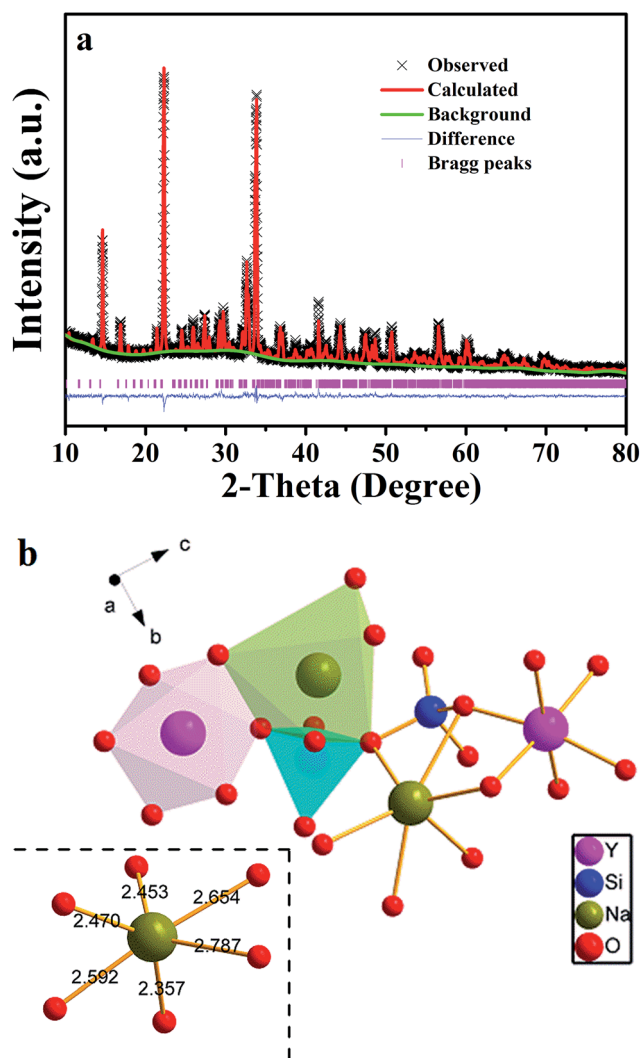
Fig. 2 (a) Powder XRD pattern of $Na_3YSi_3O_9:0.03Ce^{3+}$ with its corresponding Rietveld refinement (red solid line) and residuals (blue line in the bottom); (b) the coordination sphere of six-coordinated Na^+ in the $Na_3YSi_3O_9$ host matrix.
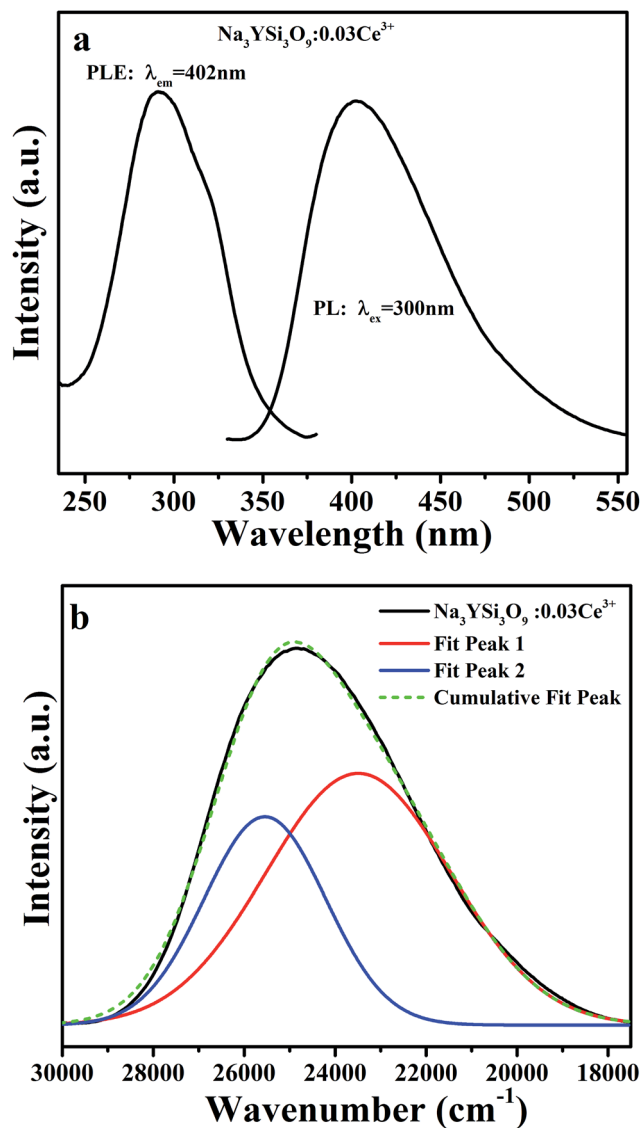

Fig. 3 (a) The PL (λ_{ex} = 300 nm) and PLE (λ_{em} = 402 nm) spectra of $Na_3YSi_3O_9:0.03Ce^{3+}$; (b) the PL spectrum of $Na_3YSi_3O_9:0.03Ce^{3+}$ and its Gaussian components.

Table 1 Rietveld refinement and crystal date for $Na_3YSi_3O_9$ and $Na_3YSi_3O_9:0.03Ce^{3+}$

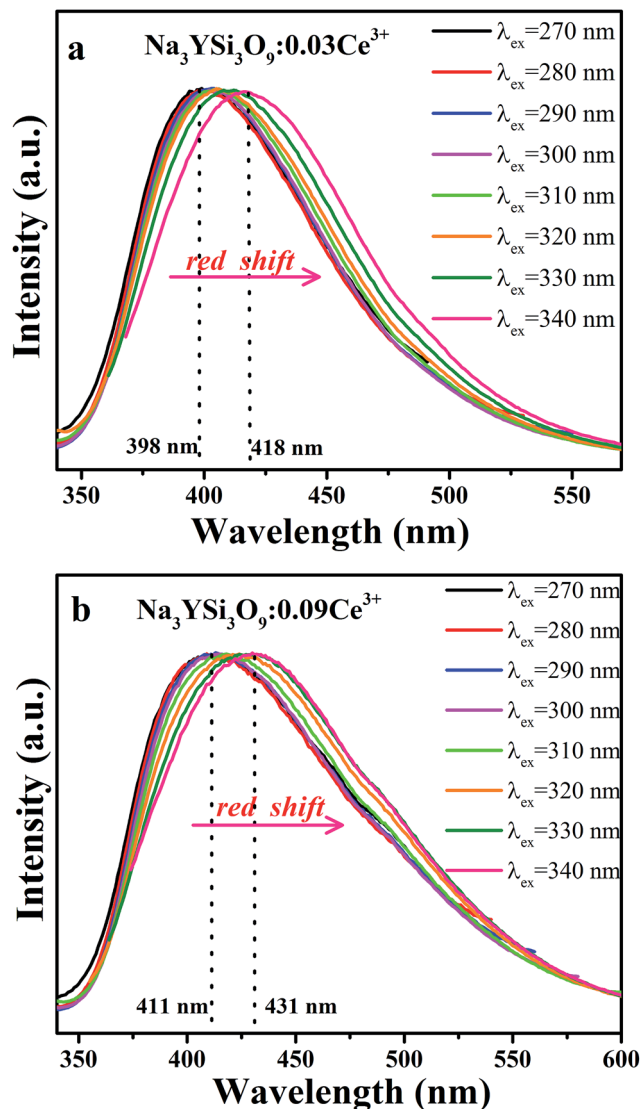| Compound	Standard $Na_3YSi_3O_9$	Un-doped $Na_3YSi_3O_9$	$Na_3YSi_3O_9:0.03Ce^{3+}$
Symmetry	Orthorhombic	Orthorhombic	Orthorhombic
Space group	$P2_12_12_1$	$P2_12_12_1$	$P2_12_12_1$
a (Å)	15.0330	15.0384(1)	15.0363(4)
b (Å)	15.1420	15.1478(0)	15.1427(5)
c (Å)	15.2130	15.2135(9)	15.2095(3)
α (deg)	90	90	90
β (deg)	90	90	90
γ (deg)	90	90	90
V (Å^3)	3462.93	3465.64(0)	3463.08(5)
Z	16	16	16
$R_{wp}\%$	—	17.01	17.37
$R_p\%$	—	12.95	12.81
χ^2	—	6.560	7.048

Fig. 4 (a) The normalized PL spectra of Na$_3$YSi$_3$O$_9$:0.03Ce^{3+} excited with different excitation wavelengths; (b) the normalized PL spectra of Na$_3$YSi$_3$O$_9$:0.09Ce^{3+} excited with different excitation wavelengths.

Fig. 5 (a) The PL spectra of Na$_3$YSi$_3$O$_9$:xCe^{3+} (x = 0.002, 0.01, 0.03, 0.05, 0.07, 0.09, 0.11) phosphors under 300 nm excitation; (b) the normalized PL spectra of Na$_3$YSi$_3$O$_9$:xCe^{3+} excited under 300 nm.

transition of Ce^{3+} is caused from two contributions, namely, centroid shift (ε_c) and crystal field splitting (ε_{cfs}),[15,28] as illustrated in Fig. 6. The centroid shift is the shift of 5d centroid energy relative to free Ce^{3+} ions, which is 6.35 eV (51 230 cm^{-1}), while crystal field splitting is the energy difference between the lowest and highest 5d-level.[15,28] The 4f–5d transition energy of Ce^{3+} ions doped in Na$_3$YSi$_3$O$_9$ can be written as:[27]

$$E_{fd}(3+,A) = E_{fd}(3+,free) - D(3+,A) \tag{1}$$

where $E_{fd}(3+,free)$ is the energy for the first 4f–5d transition of free Ce^{3+} ions. The relationship between $D(3+,A)$ and $\varepsilon_c(3+,A)$ and $\varepsilon_{cfs}(3+,A)$ can be related as:[29]

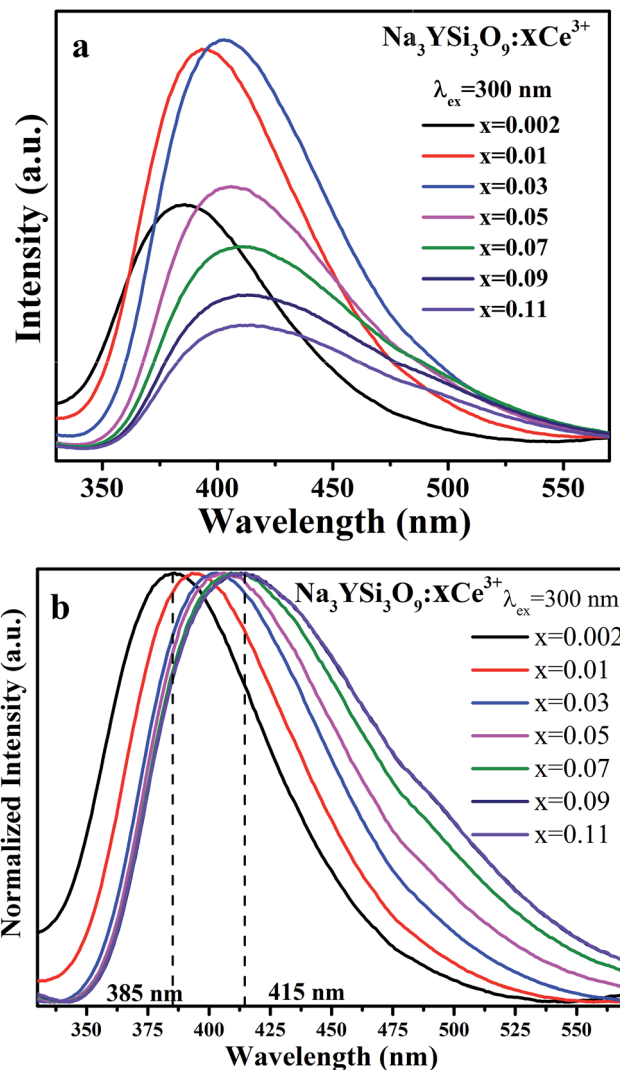$$D(3+,A) = \varepsilon_c(3+,A) + \frac{\varepsilon_{cfs}(3+,A)}{r(3+,A)} - 1890 \ \text{cm}^{-1} \tag{2}$$

where $1/r(3+,A)$ is the fraction of ε_{cfs} that adds to the red shift, and which depends on the type of polyhedron.

Origin of the centroid shift is very complicated and determined by chemical (covalence) and physical (polarizability) properties of the anions coordinating Ce^{3+}.[27,28] Based on the model that describes the correlated motion between 5d electron and ligand electrons, the 5d centroid shift for Ce^{3+} can be given as:[15,30]

$$\varepsilon_c = 1.79 \times 10^{13} \sum_{i=1}^{N} \frac{\alpha_{sp}^i}{(R_i - 0.6\Delta R)^6} \tag{3}$$

where R_i is the distance between Ce^{3+} and anion i in the undistorted lattice. The summation is over all N anions that coordinate Ce^{3+} and 0.6ΔR is a correction for lattice relaxation around Ce^{3+}. Note α_{sp}^i (10^{-30} m^{-3}) is the spectroscopic polarizability of anion i, and it is an important parameter that includes the effects of correlated motion and covalence between
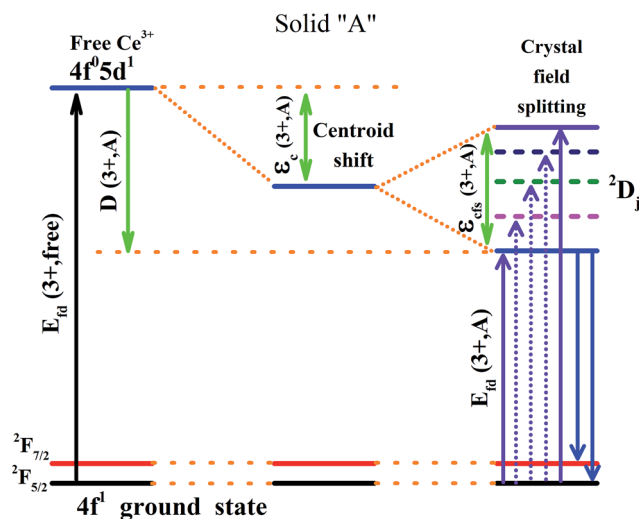
Fig. 6 Schematic diagram of the centroid shift $\varepsilon_c(3+,A)$, crystal field splitting $\varepsilon_{cfs}(3+,A)$, red shift $D(3+,A)$ and emission of Ce^{3+} in a certain compound.

Ce^{3+} and also the anions and other possible contributions to the centroid shift. For the oxides:[15,30,31]

$$\alpha_{sp}^o = 0.33 + 4.8/\chi_{av}^2 \qquad (4)$$

where χ_{av} is the weighted average of the electronegativity of the cations in the oxide compounds. Due to the electronegative defect around Ce^{3+} ions, the value of χ_{av} for Ce^{3+} in the Na_3-YSi_3O_9 would be smaller and the 5d centroid shift ε_c of Ce^{3+} is more obvious according to eqn (3) and (4). Naturally, the 4f–5d transition energy of Ce^{3+} ions with the vacancies would be lower.

Crystal field splitting is related to the shape and size of the first anion coordination polyhedron around Ce^{3+}.[27,28] There is an empirical relationship between ε_{cfs} and the average distance (R) from the central ion to its ligand anions:[15,28]

$$\varepsilon_{cfs} = \beta_{ploy}R^{-2} \qquad (5)$$

The β_{ploy} values are in the ratio of 1, 0.89, 0.79, 0.42, and 0.42 for octahedral, cubic, dodecahedral, tricapped trigonal prism, and cuboctahedral, respectively;[28] anyhow, it is a constant for $Na_3YSi_3O_9$. The ε_{cfs} would decrease with the average distance (R) increasing, as obtained from eqn (5). The smaller Ce^{3+} ions substituted in the position of six-coordinated Na^+ sites in Na_3-YSi_3O_9 leads to the shrinkage of cell volume, which then would decrease the average distance (R) and increase the strength of the crystal field. With the doping of Ce^{3+} ions, more electronegative vacancies will affect charge distribution of its chemical environment around the luminescence center Ce^{3+}. Therefore, the centroid shift of Ce^{3+} is larger and the energy of the 5d-levels of Ce^{3+} is lower. Moreover, the shrinkage effect will be more effective and the strength of the crystal field increases with Ce^{3+} ions' concentration, leading to larger energy difference between the lowest and highest 5d-level. Finally, the lowest 5d-level of Ce^{3+} ions shift down, resulting in the emissions of the

$Na_3YSi_3O_9$:xCe^{3+} red shift, too. Thus, both centroid shift and crystal field splitting play important roles in the red shift of $Na_3YSi_3O_9$:xCe^{3+} phosphors.[27]

Emission intensities increase with Ce^{3+} contents until a maximum intensity is achieved, and then the intensity begins to decrease with x beyond the critical concentration due to energy dispersion between Ce^{3+} ions, namely, a concentration quenching effect.[32] The concentration-dependent luminescence spectra are shown in Fig. 7a, and the critical concentration of Ce^{3+} in $Na_3YSi_3O_9$ is 0.03 mol. The critical distance (R_c) for energy transfer among Ce^{3+} ions is necessary to further understand the interaction mechanisms, which was often calculated by using a concentration quenching method and the relationship given by Blasse:[33]

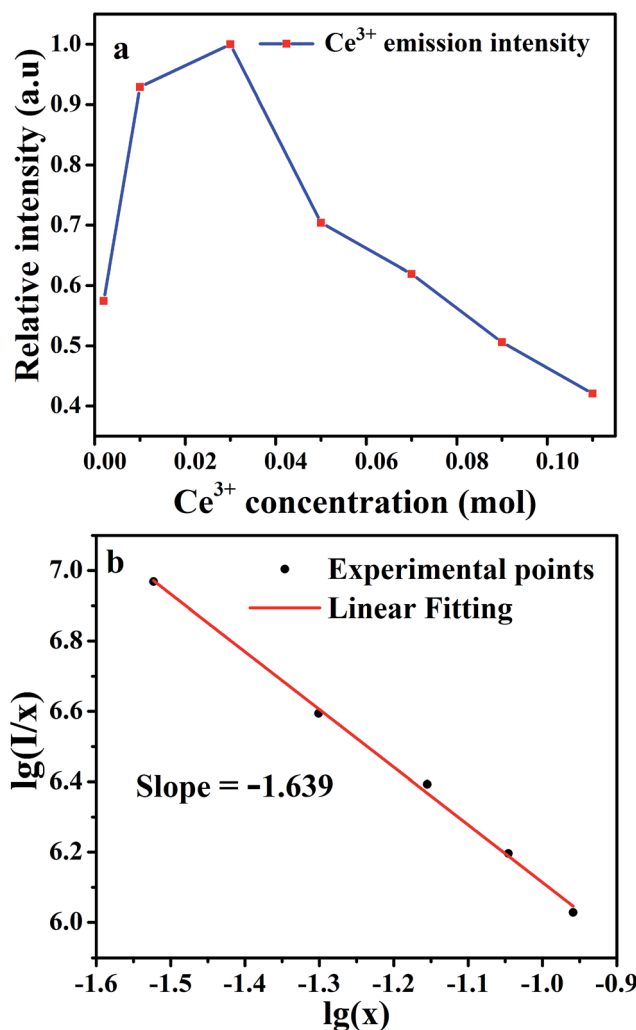$$R_c \approx 2\left(\frac{3V}{4\pi x_c N}\right)^{\frac{1}{3}} \qquad (6)$$

Fig. 7 (a) The dependence of Ce^{3+} emission intensity as a function of the Ce^{3+} content; (b) linear fitting of the relationship of $lg(I/x)$ vs. $lg(x)$ in $Na_3YSi_3O_9$:xCe^{3+} ($x = 0.002–0.11$) phosphors beyond the quenching concentration.

where V is the volume of the unit cell, x_c is the critical concentration, and N is the number of cations in the unit cell. Herein, the values are $V = 3463.08$ Å^3, $x_c = 0.03$, and $N = 48$. Thus, the R_c of Ce^{3+} was calculated to be 16.623 Å. There are three mechanisms for the nonradiative energy transfer: exchange interaction, radiation reabsorption, and electric multipolar interaction.[34] Owing to the typical critical distance of the exchange interaction being about 5 Å, the exchange interaction only fits the energy transfer of forbidden transitions.[35,36] Therefore, the electric multipolar interactions are dominant in the energy transfer process. According to Dexter's theory, the mechanism of the interaction between Ce^{3+} ions can be expressed by the following equation:[35,37]

$$\frac{I}{x} = K\left[1 + \beta(x)^{\frac{\theta}{3}}\right]^{-1} \quad (7)$$

in which x is the activator concentration, not less than the critical concentration, I/x is the emission intensity (I) per activator concentration (x), and k and β are constants for the same excitation condition for a given host lattice. θ is a function of electric multipolar character and $\theta = 6, 8, 10$ corresponds to dipole–dipole (d–d), dipole–quadrupole (d–q), and quadrupole–quadrupole (q–q) interactions, respectively. As represented in Fig. 7b, the correlation between lg(I/x) and lg(x) can be fitted linearly with a slope of -1.639 equaling to $-\frac{\theta}{3}$. The θ value is determined to be 4.917, which is close to 6. Therefore, the concentration quenching mechanism of Na$_3$YSi$_3$O$_9$:xCe^{3+} is mainly accounted for by a dipole–dipole interaction.

To further explore the energy transfer process, the decay curves of Ce^{3+} ions in Na$_3$YSi$_3$O$_9$:xCe^{3+} phosphors by monitoring 402 nm excited by 320 nm were also measured (Fig. 8). As discussed above, the electronegative vacancies will affect the interaction of the charge distribution with its chemical environment around Ce^{3+} ions, which would modify fluorescence

Fig. 8 Decay curves and lifetimes of Ce^{3+} emission in Na$_3$YSi$_3$O$_9$:xCe^{3+} ($x = 0.002$–0.09) phosphors (excited at 320 nm, monitored at 402 nm).

dynamics of the Ce^{3+} ions. Results revealed that the fluorescence decays deviated from the single-exponential rule, and this deviation is more obvious with doping Ce^{3+} content. The decay curves were fitted with a second-order exponential decay model as:[24]

$$I = A_1 \exp(-t/\tau_1) + A_2 \exp(-t/\tau_2) \quad (8)$$

where I is the luminescence intensity, A_1 and A_2 are constants, and τ_1 and τ_2 are the short and long lifetimes for exponential components. The average decay time τ can be calculated as:

$$\tau = (A_1\tau_1^2 + A_1\tau_2^2)/(A_1\tau_1 + A_1\tau_2) \quad (9)$$

The average decay times τ are calculated to be 36.734, 33.862, 31.921, 27.442, 25.806, and 23.233 ns for Na$_3$YSi$_3$O$_9$:xCe^{3+} ($x = 0.002, 0.01, 0.03, 0.05, 0.07$, and 0.09) phosphors. All the results show that the lifetime τ of the 5d^1–4f^1 transitions of Ce^{3+} ions in Na$_3$YSi$_3$O$_9$ decreases with Ce^{3+} concentration, indicating energy dispersion between Ce^{3+} ions. The measured lifetime is also related to the total relaxation rate expressed as:[11]

$$1/\tau = 1/\tau_0 + A_{nr} + P_t \quad (10)$$

where τ_0 is the radiative lifetime, A_{nr} is the nonradiative rate due to multi-phonon relaxation, and P_t is the energy transfer rate between Ce^{3+} ions. With increasing Ce^{3+} concentration, the distance between Ce^{3+} ions decreases. Then, both the Ce^{3+}–Ce^{3+} energy transfer rate (corresponding to P_t) and the probability of energy transfer to quenching sites (corresponding to A_{nr}) increase. As a result, the lifetimes are shortened with increasing concentrations of Ce^{3+}.

3.3 Thermal stability of Na$_3$YSi$_3$O$_9$:Ce^{3+} phosphor

Thermal stability is important for practical applications due to its significant influence on light output and CRI. Temperature-dependent PL spectra of the Na$_3$YSi$_3$O$_9$:0.03Ce^{3+} phosphor excited by 300 nm are depicted in Fig. 9. When the temperature increased from 25 °C to 250 °C, the luminescence intensity decreased gradually to 56.97% at 100 °C. Thermal stability of Na$_3$YSi$_3$O$_9$:0.03Ce^{3+} and commercial BAM:Eu^{2+} is shown in the inset of Fig. 9. Thermal quenching can be explained by a configuration coordinate diagram. At high temperature, the electron–phonon interaction is intensive, and the electrons in the 5d excited state could be thermally activated to the 4f ground state through the crossing point between the excited state and the ground state. The nonradiative thermal relaxation process results in decreased luminescence intensity.[38] The full width at the half maximum (FWHM) of PL spectrum increases with the temperature, which can be described by using the Boltzmann distribution:[39]

$$\text{FWHM}(T) = W_0 \times \sqrt{\coth\frac{h\nu}{2kT}} \quad (11)$$

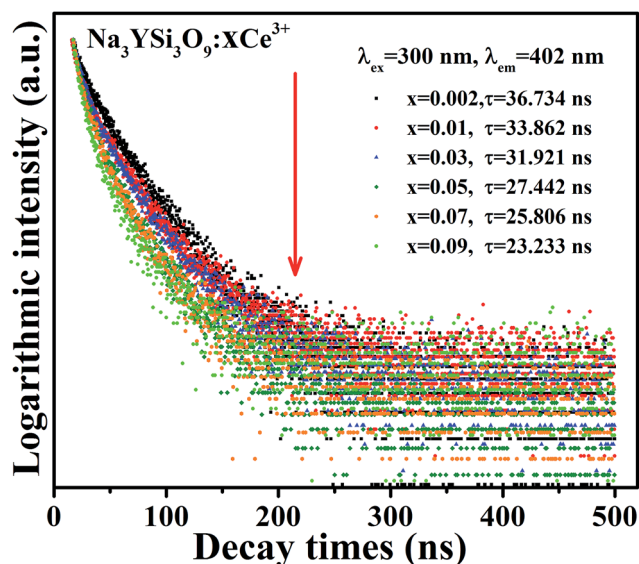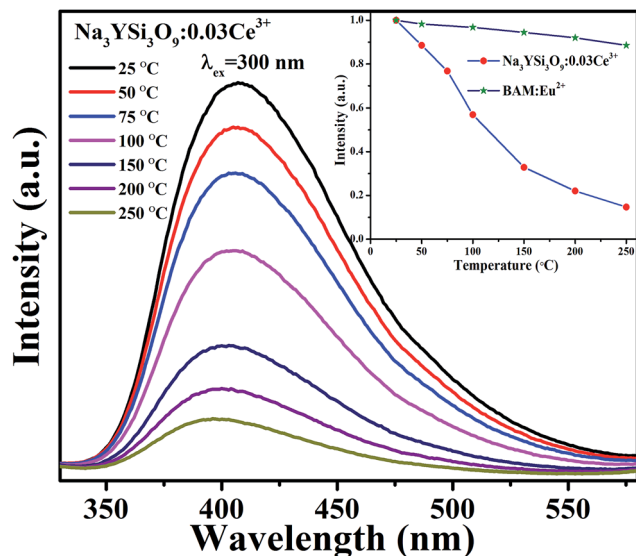$$W_0 = \sqrt{8\ln 2} \times h\nu \times \sqrt{s} \quad (12)$$

Fig. 9 Temperature-dependent PL spectra of $Na_3YSi_3O_9$:$0.03Ce^{3+}$ phosphor; the inset shows the emission of $Na_3YSi_3O_9$:$0.03Ce^{3+}$ and the commercial BAM as a function of temperature when excited at 300 nm.

where W_0 is the FWHM at 0 K, $h\nu$ represents the vibrational phonon energy which interacts with the electronic transitions, S means the Huang–Rhys parameter, and k is the Boltzmann constant. It is assumed that $h\nu$ is the same for both 4f ground state and 5d excited state of Ce^{3+} ions. When the temperature increases, the electron–phonon interaction becomes dominate and the excited electrons spread to higher vibration levels, and then, the increasing transition from different levels result in the increase of FWHM.[36]

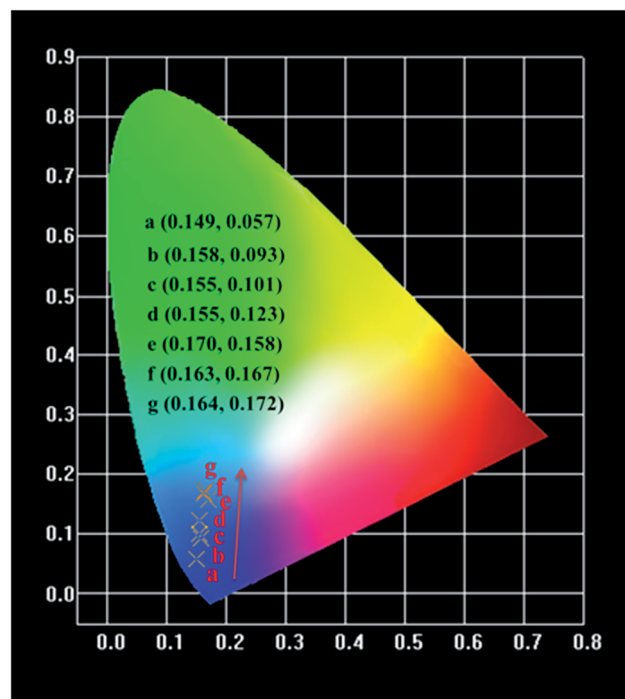To further investigate the relationship of emission intensity with temperature, the activation energy (ΔE) for

Fig. 10 The linear fitting of $\ln[(I_0/I_t) - 1]$ vs. $1/kT$ for thermal quenching of $Na_3YSi_3O_9$:$0.03Ce^{3+}$; the inset shows the configuration coordinate diagram for an explanation of thermal quenching.

Fig. 11 CIE chromaticity diagram of $Na_3YSi_3O_9$:xCe^{3+} ($x = 0.002–0.11$) phosphors excited at 300 nm.

thermal quenching can be estimated using the Arrhenius equation:[40]

$$I_T = \frac{I_0}{1 + c \exp(-\Delta E/kT)} \quad (13)$$

where I_0 is the initial intensity, I_T is the intensity at different temperatures, c is a constant, ΔE is the activation energy for thermal quenching, and k is the Boltzmann constant (8.62×10^{-5} eV). According to the equation, the activation energy ΔE is calculated to be 0.277 eV by the relationship of $\ln[(I_0/I_T) - 1]$ against $1/kT$, as shown in Fig. 10.

3.4 CIE color coordinates

The variations of Commission International de L' Eclairage (CIE) chromaticity coordinates of the $Na_3YSi_3O_9$:xCe^{3+} ($x = 0.002, 0.01, 0.03, 0.05, 0.07, 0.09,$ and 0.11) phosphors are determined based on the PL spectra excited at 300 nm (Fig. 11). The CIE chromaticity diagram is tuned from (0.149, 0.057) to (0.164, 0.172) with increasing concentrations of Ce^{3+} ions from 0.002 to 0.11. The result indicates that the chromaticity coordinates of $Na_3YSi_3O_9$:xCe^{3+} phosphors can be modulated over a wide range by appropriately changing the concentrations.

4. Conclusion

In summary, a serious of blue-emitting $Na_3YSi_3O_9$:Ce^{3+} phosphors were synthesized *via* a traditional solid-state reaction. Results of X-ray diffraction (XRD) and Rietveld refinement analysis indicate that the doping of Ce^{3+} ions did not cause any impurities in $Na_3YSi_3O_9$. Concentration quenching of
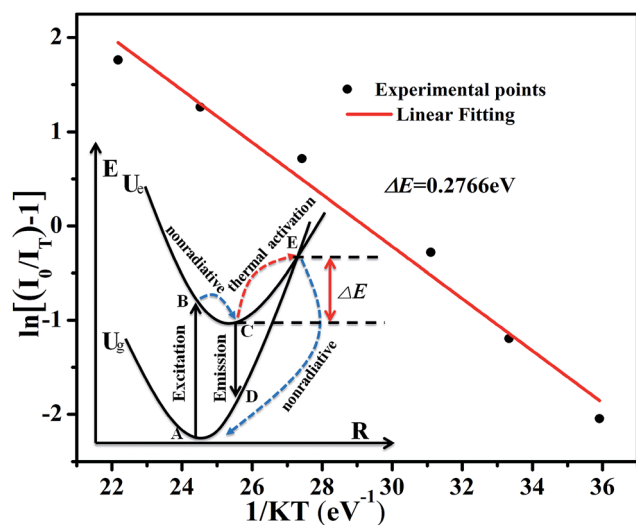
$Na_3YSi_3O_9:Ce^{3+}$ occurs and the critical quenching concentration was determined to be about 3 mol%. The energy transfer critical distance was calculated to be about 16.626 Å. The corresponding quenching mechanism was verified to be a dipole–dipole interaction. The activation energy ΔE of Ce^{3+} ion was calculated to be 0.277 eV. The CIE chromaticity coordinates of $Na_3YSi_3O_9:xCe^{3+}$ phosphors can be tuned in a wide range from (0.149, 0.057) to (0.164, 0.172) with Ce^{3+} ions increasing from 0.002 to 0.11. Upon 300 nm excitation, the emission peaks of $Na_3YSi_3O_9:0.03Ce^{3+}$ phosphors shifted to a longer wavelength of 20 nm as the Ce^{3+} concentration was determined and to 30 nm when Ce^{3+} concentration increased from 0.002 to 0.11. The spectral red-shift phenomenon is explained by a centroid shift and crystal field splitting. Therefore, some novel phosphors, especially in solid solution, may be prepared by combining centroid shift and crystal field splitting to adjust an emission for application.

Acknowledgements

References

1 M. R. Krames, O. B. Shchekin, R. Mueller-Mach, G. O. Mueller, L. Zhou, G. Harbersand and M. G. Craford, *J. Disp. Technol.*, 2007, **3**(2), 160–175.

2 T. G. Kim, H. S. Lee, C. C. Lin, T. Kim, R. S. Liu, T. S. Chan and S. J. Im, *Appl. Phys. Lett.*, 2010, **96**(6), 061904.

3 K. S. Sohn, D. H. Park, S. H. Cho, J. S. Kwak and J. S. Kim, *Chem. Mater.*, 2006, **18**(7), 1768–1772.

4 S. Lee and S. Y. Seo, *J. Electrochem. Soc.*, 2002, **149**(11), J85–J88.

5 A. Setlur, *Electrochem. Soc. Interface*, 2009, **16**(4), 32–36.

6 Z. Hao, J. Zhang, X. Zhang, X. Sun, Y. Luo, S. Lu and X. Wang, *Appl. Phys. Lett.*, 2007, **90**, 261113.

7 Y. Shi, Y. Wang, Y. Wen, Z. Zhao, B. Liu and Z. Yang, *Opt. Express*, 2012, **20**(19), 21656–21664.

8 S. J. Gwak, P. Arunkumar and W. B. Im, *J. Phys. Chem. C*, 2014, **118**(5), 2686–2692.

9 V. R. Bandi, B. K. Grandhe, K. Jang, S. S. Kim, D. S. Shin, Y. I. Lee, J. M. Lim and T. Song, *J. Lumin.*, 2011, **131**(11), 2414–2418.

10 D. Ananias, L. D. Carlos and J. Rocha, *Opt. Mater.*, 2006, **28**(6), 582–586.

11 C. H. Kim, H. L. Park and S. Mho, *Solid State Commun.*, 1997, **101**(2), 109–113.

12 W. Zhao, S. An, B. Fan and S. Li, *J. Lumin.*, 2013, **143**, 71–74.

13 Y. Q. Li, N. Hirosaki, R. J. Xie, T. Takeda and M. Mitomo, *Chem. Mater.*, 2008, **20**(21), 6704–6714.

14 Y. He, J. Zhang, W. Zhou, J. Han, Z. Qiu, L. Yu, C. Rong and S. Lian, *J. Am. Ceram. Soc.*, 2014, **97**(5), 1517–1522.

15 M. Shang, G. Li, D. Geng, D. Yang, X. Kang, Y. Zhang, H. Lian and J. Lin, *J. Phys. Chem. C*, 2012, **116**(18), 10222–10231.

16 S. P. Lee, C. H. Huang and T. M. Chen, *J. Mater. Chem. C*, 2014, **2**(42), 8925–8931.

17 W. B. Im, N. N. Fellows, S. P. DenBaars, R. Seshadri and Y. I. Kim, *Chem. Mater.*, 2009, **21**(13), 2957–2966.

18 W. B. Im, K. Page, S. P. DenBaars and R. Seshadri, *J. Mater. Chem.*, 2009, **19**(46), 8761–8766.

19 X. Zhang and M. Gong, *J. Alloys Compd.*, 2011, **509**(6), 2850–2855.

20 A. C. Larson and R. B. Von Dreele, *Los Alamos National Laboratory Report LAUR*, 1994, pp. 86–748.

21 G. Blasse and B. C. Grabmaier, *Luminescent Materials*, Springer-Verlag, Berlin, 1994.

22 W. B. Dai, *RSC Adv.*, 2014, **4**(22), 11206–11215.

23 P. Dorenbos, *J. Lumin.*, 2013, **135**, 93–104.

24 C. H. Huang, P. J. Wu, J. F. Lee and T. M. Chen, *J. Mater. Chem.*, 2011, **21**(28), 10489–10495.

25 P. D. Rack and P. H. Holloway, *Mater. Sci. Eng., R*, 1998, **21**(4), 171–219.

26 N. Guo, Y. Zheng, Y. Jia, H. Qiao and H. You, *J. Phys. Chem. C*, 2011, **116**(1), 1329–1334.

27 S. Shionoya, W. M. Yen and H. Yamamoto, *Phosphor Handbook*, CRC press, 2006.

28 P. Dorenbos, *J. Lumin.*, 2002, **99**(3), 283–299.

29 P. Dorenbos, *Phys. Rev. B: Condens. Matter Mater. Phys.*, 2000, **62**(23), 15640–15649.

30 P. Dorenbos, *J. Lumin.*, 2003, **105**(2), 117–119.

31 T. Wang, Z. Xia, Q. Xiang, S. Qin and Q. Liu, *J. Lumin.*, 2015, **166**, 106–110.

32 W. B. Im, S. Brinkley, J. Hu, A. Mikhailovsky, S. P. Denbaars and R. Seshadri, *Chem. Mater.*, 2010, **22**(9), 2842–2849.

33 G. Blasse, *Philips Res. Rep.*, 1969, **24**(2), 131–144.

34 J. Zhong, W. Zhuang, X. Xing, R. Liu, Y. Li, Y. Liu and Y. Hu, *J. Phys. Chem. C*, 2015, **119**(10), 5562–5569.

35 D. L. Dexter, *J. Chem. Phys.*, 1953, **21**(5), 836–850.

36 J. Chen, Y. Liu, L. Mei, H. Liu, M. Fang and Z. Huang, *Sci. Rep.*, 2015, **5**, 9673.

37 G. Blasse, *Phys. Lett. A*, 1968, **28**(6), 444–445.

38 M. Jiao, Y. Jia, W. Lü, W. Lv, Q. Zhao, B. Shao and H. You, *J. Mater. Chem. C*, 2014, **2**(21), 4304–4311.

39 P. Dorenbos, *J. Lumin.*, 2003, **104**(4), 239–260.

40 C. H. Huang and T. M. Chen, *Inorg. Chem.*, 2011, **50**(12), 5725–5730.